Research Article

$[Mo_2O_2S_8]^{2-}$ small molecule dimer as a basis for hydrogen evolution reaction (HER) catalyst materials

Danielle N. Chirdon[1] · Remy F. Lalisse[1] · Jiaonan Sun[1] · Songwei Zhang[1] · Benjamin R. Garrett[1] · Christopher M. Hadad[1] · Yiying Wu[1]

Received: 25 January 2020 / Accepted: 6 April 2020 / Published online: 13 April 2020

Abstract

Molybdenum sulfides have emerged as promising, low cost alternatives to platinum for catalysis of the electrochemical hydrogen evolution reaction (HER). A wide variety of sulfides already achieve impressive catalysis, but further development could be enabled by an understanding of the relative activities of different sulfur sites. To contribute towards a better understanding, the small molecule dimer $[Mo_2O_2S_8]^{2-}$, which is rich in terminal and unsaturated sulfur, has been investigated for HER. Homogeneous catalysis has been attempted in acidified DMF but is precluded by electrodeposition. The resulting deposit ultimately proves to be an active heterogeneous HER catalyst in aqueous acid and is compared to dropcasts of the molecular dimer which are also HER catalysts. XPS elucidates the end structures of the electrodeposits and dropcasts showing a shift away from molecular features in both cases. Investigation of HER performance reveals that the activity of both dimer-based heterogeneous catalysts lags behind that of other reported molybdenum sulfides. However, detailed performance comparisons allow for consideration of key design parameters. Density functional theory calculations are presented for the reduced molecular dimer as well as possible molecular catalytic pathways. These give insight into the cathodic structural transformations of the dimer as well as the observation of heterogeneous but not homogeneous catalysis.

Graphic abstract

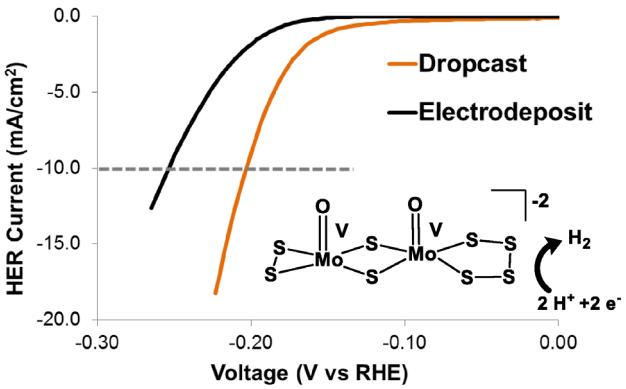

Electronic supplementary material The online version of this article (https://doi.org/10.1007/s42452-020-2706-3) contains supplementary material, which is available to authorized users.

✉ Christopher M. Hadad, hadad.1@osu.edu; ✉ Yiying Wu, wu.531@osu.edu | [1]Department of Chemistry and Biochemistry, The Ohio State University, 100 West 18th Avenue, Columbus, OH 43210, USA.

Keywords Hydrogen evolution reaction · Molybdenum sulfides · MoS_2 mimics · Sulfur active sites · Electrodeposition · Heterogeneous catalysis

1 Introduction

Efficient electrochemical reduction of protons to molecular hydrogen is critical for realization of more sustainable energy practices. The process is a required half reaction for conversion of solar energy into useful hydrogen fuel via water splitting devices [1–3]. Moreover, when driven by renewable electricity, the electrochemical hydrogen evolution reaction (HER) can supply hydrogen for fertilizer, petrochemical, and other industries [4, 5], thereby serving as a clean, carbon-free alternative to steam reforming [6, 7]. However, for electrochemical HER to be efficient enough for large scale or solar-driven applications, highly active catalysts are needed to lower its activation energy barrier and to facilitate the kinetics [1–3]. Platinum has traditionally been the best HER catalyst, but cheaper, more earth abundant catalysts are needed to ensure scalability and economic viability [8].

Among cheap alternatives to platinum, molybdenum sulfide materials have been pursued intensely [9, 10]. Interest in these materials began in 2005 when Hinnemann et al. determined that the triangular edges of bulk MoS_2 where Mo binds to terminal S_2^{2-} (Fig. 1) are energetically similar to the active sites in hydrogen-evolving enzymes [11]. In crystalline MoS_2 though, only the limited edge sites are active while the bulk basal planes are inert, leading to poor activity per gram or unit area [12]. Recent efforts have made tremendous progress in building from bulk MoS_2 towards more practical HER catalysts through two major approaches: (1) enhancing the activity of each available catalytic site and (2) creating a higher density of active sites.

To pursue the first approach involving enhanced site activity, metal dopants have been used to optimize ΔG for hydrogen adsorption at molybdenum sulfide edges [13, 14]. Moreover, proton accessibility and electrical conductivity to those edges have been improved by forming ultrathin layers [15–18] and composites with conductive materials [19–23], respectively. In terms of the second approach regarding site density, work has largely centered on replacing typically sheet-like and crystalline MoS_2 with new morphologies. High surface area constructs, such as highly dispersed nanoparticles [24, 25] and porous networks [26–29], maximize the edge to bulk ratio in order to obtain substantial HER currents. Amorphous MoS_x morphologies offer a large numbers of defects as compared to crystalline MoS_2, thereby creating more active sulfur moieties [30]. Strong performance can also be obtained with small molecule complexes [31–33] or clusters [34, 35], enabling precise engineering of the numbers and types of sulfur ligands per molybdenum center.

Of course, in any approach to improving catalysis, knowledge of the true nature of the active site is critical for informed material design. Computations [36] and spectroscopy [37] both point to sulfur as the site of proton binding in molybdenum sulfides, and as noted earlier, terminal S_2^{2-} has already been identified as active in bulk MoS_2 [12].[1] Yet, with the advent of new amorphous deposits and clusters having many forms of sulfur (Fig. 1), some questions have emerged regarding which sulfur provides the highest activity. In-situ x-ray absorption spectroscopy has been used by Yano and co-workers to implicate terminal S_2^{2-} as active in amorphous MoS_x [40]. In-situ Raman studies on the same material alternatively indicate that terminal groups diminish during HER leaving unsaturated S^{2-} and bridging S_2^{2-} as the likely active sites [37]. Li and co-workers, meanwhile, have attributed the outstanding performance of their Mo_3S_{13} and MoS_x/pyrrole deposits to an overabundance of sulfur, especially bridging S_2^{2-} and apical S^{2-}, moieties marked by relatively high XPS binding energies [23, 41, 42].

In light of this ongoing discussion, we became interested in the anionic molybdenum dimer, $[Mo_2O_2S_8]^{2-}$ (Fig. 1b), as a possible HER catalyst. This dimer has only terminal and unsaturated sulfur motifs possibly allowing further commentary on their HER performance in isolation from other sulfur types. Moreover, the dimer is rich in sulfur having the active sites of crystalline MoS_2 without the inactive basal plane, and this may allow a high activity (i.e. high turn-over frequency) per molybdenum center. The dimer has been previously reported mainly as a synthetic precursor for organo-molybdenum complexes [43, 44]. Here, it is reported as a precursor for an electrodeposited MoS_x material and as an effective dropcast HER catalyst. DFT calculations evaluate possible HER reaction pathways for the molecular dimer, thereby giving insight into morphology changes observed during HER as well as the observance of heterogeneous catalysis by dimer products, but not homogeneous catalysis by the dimer itself.

[1] For more information on the nature of the active MoS_2 edges see: [38, 39].

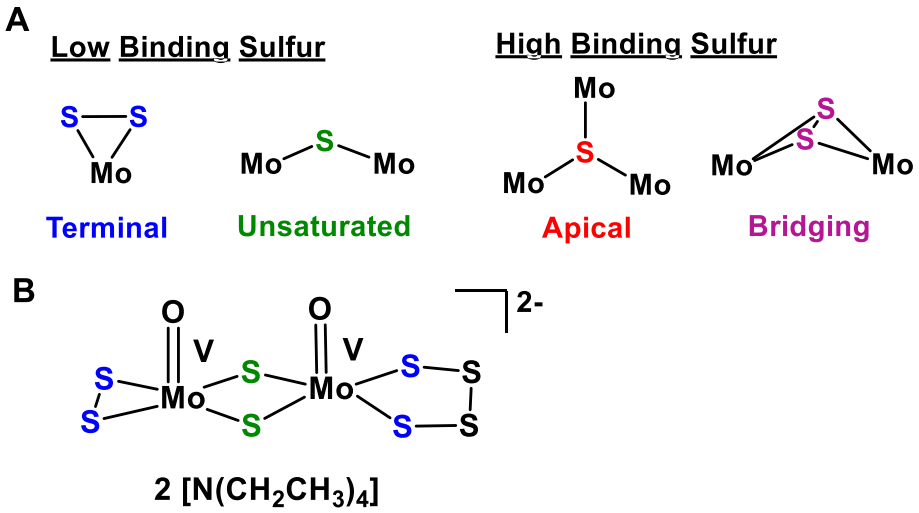

Fig. 1 **a** Sulfur motifs found in molybdenum sulfide HER electrocatalyst materials. Motifs are grouped according to their relative electron binding energy observed in XPS. **b** Structure of $[Mo_2O_2S_8]^{2-}$ dimer with unsaturated sulfur in green and terminal sulfur in blue

2 Results and discussion

2.1 Electrochemistry

The anionic dimer $[Mo_2O_2S_8]^{2-}$ was readily synthesized from heptamolybdate via a room temperature, aerobic reaction described by Coucouvanis et al. [44]. Homogeneous electrochemistry of the dimer in DMF solution has been previously probed in a narrow potential window revealing two reductions [45]. Further work here though suggests that these reductions actually belong to an oxidized impurity as they are minor in comparison to pronounced processes observed at more extended potentials (Figure S1). The pronounced redox processes include two highly cathodic reductions (−2.39 V, −2.67 V vs Fc/Fc^+) which are diffusion controlled and irreversible over a wide range of scan rates. Also included are two overlapping, irreversible oxidations (0.09 V, 0.21 V vs Fc/Fc^+) possibly representing the V/VI redox couple [46][2] for each of the dimer's two similar molybdenum(V) centers. All observed redox processes cycle reproducibly without leaving any visible deposit on the electrode.

2.2 Electrodeposition

Beyond basic electrochemistry, we were interested in exploring the Mo dimer's homogeneous HER catalysis. We have previously observed stable catalysis by organometallic molybdenum-sulfide complexes in acidified organic solution [32, 33], but at the same time, we have been limited by instability in our efforts to use molybdenum cubanes as homogeneous catalysts for water-reducing photocathodes [47]. Here, addition of trifluoroacetic acid (TFA) as a proton source to the Mo dimer in DMF does not produce the anodic shifting and current amplification of an existing reduction which often marks homogeneous electrochemical catalysis. Instead, original reductions remain intact while a new reduction appears at significantly more anodic potentials (−1.79 V vs Fc/Fc^+, Fig. 2). With successive scanning, this signal constantly shifts ultimately proving to arise from a proton-assisted deposition which leaves a visible coating on the electrode. Protons are clearly critical to the deposition, but any involvement of a ground state complex between protons and Mo dimer can be ruled out as UV–vis spectroscopy shows that the spectral signal of the dimer in DMF is not significantly altered by introduction of acid (Figure S2).

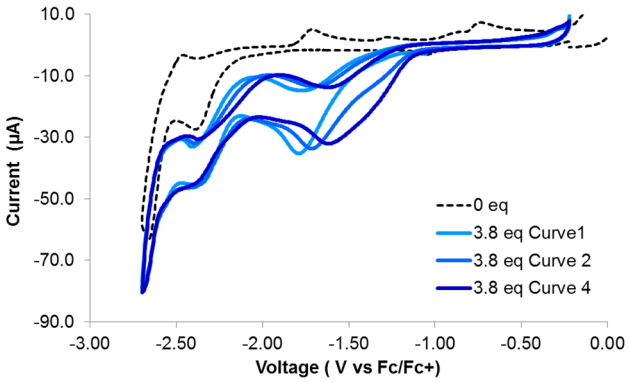

Fig. 2 Homogeneous redox chemistry of $[Mo_2O_2S_8]^{2-}$ dimer (2 mM) in 0.1 M $TBAPF_6$/DMF and successive cycles after addition of 3.8 equivalents of TFA. Voltammetry was conducted under argon at 50 mV/s with a glassy carbon working electrode (0.071 cm^2), platinum counter electrode, and $Ag/AgNO_3$ reference

Deposition from the Mo dimer is accompanied by the growth of another cathodic process at still more positive

[2] This assignment is based on the common observation of a facile V/VI redox couple for Mo in enzyme centers as in Ref [46].

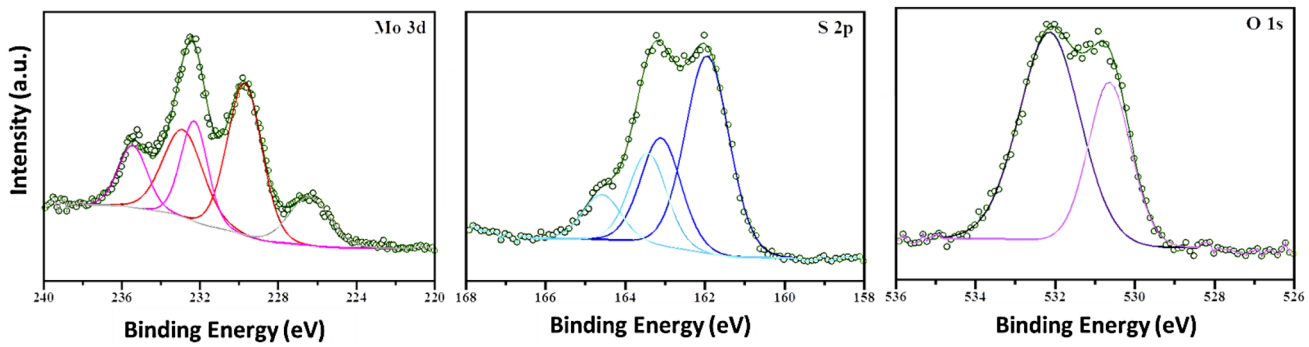

Fig. 3 XPS results in the Mo 3d (left), S 2p (middle), and O 1 s (right) regions for an electrodeposit formed from $[Mo_2O_2S_8]^{2-}$ dimer. The deposit was formed on FTO from 3 mM dimer in DMF with 18 equivalents of TFA using controlled potential coulometry at −1.9 V versus Fc/Fc^+

potentials near −1.4 V versus Fc/Fc^+. Probing the deposit itself in fresh DMF with and without acid (Figure S3) allows for assignment of this process as proton reduction by the deposit. Thus, while the Mo dimer is not a homogeneous HER catalyst like organometallic Mo complexes, it is perhaps not surprisingly a precursor for a heterogeneous catalyst as are similar MoS_4^{2-} and $Mo_3S_{13}^{2-}$ inorganic anions [41, 42].

Bulk electrolysis of Mo dimer at the deposition potential with excess TFA (18 equivalents) enables growth of uniform films on both glassy carbon and fluorine-doped tin oxide (FTO) substrates (Figure S4). On FTO, molybdenum loading determined by atomic emission spectroscopy increases at a rate of 29 nmol Mo per coulomb ± 10%. The typical deposition charge used here was 3.8–4.5 C/cm^2, giving films with a Mo loading in the range 110–131 nmol Mo/cm^2 and thickness of ~ 0.34 mm/cm^2 based on profilometry.

To probe the nature of the deposited materials, XPS characterization was employed and critical spectral regions are shown in Fig. 3. The Mo region contains no signal for molybdenum in the +5 oxidation state ($3d_{3/2}$ = 234.1 eV and $3d_{5/2}$ = 230.9 eV) observed for the small molecule dimer in dropcastings (vide infra). Instead, a prominent doublet appears at 232.87 eV ($3d_{3/2}$)/229.72 eV ($3d_{5/2}$) and is consistent with Mo(IV) found in crystalline MoS_2 as well as amorphous electrodeposited MoS_x [30, 37, 48]. One other doublet appears in the region at higher binding energies (235.44 eV/232.29 eV) and can be ascribed to Mo(VI) in MoO_3. This signal is commonly observed in electrodeposited amorphous MoS_x representing an air oxidized surface layer [37, 48]. The sulfur region for the dimer electrodeposit indicates two types of sulfur with doublets at 163.10 ($2p_{1/2}$)/161.91 ($2p_{3/2}$) and 164.59 ($2p_{1/2}$)/163.43 ($2p_{3/2}$). The doublet at lower binding energies represents terminal S_2^{2-} and unsaturated S^{2-} expected from the dimer structure. The higher binding doublet is indicative of bridging and apical moieties which do not appear in the dimer or crystalline MoS_2 but are pervasive in electrodeposits including Mo_3S_{13} [41, 42] and amorphous MoS_2 or MoS_3 [37, 48]. The ratio of low to high binding sulfur significantly favors the low binding terminal/unsaturated moieties and is nearly identical to the ratio seen in amorphous MoS_2 [48].

In fact, on the whole, the XPS for the deposit reported here is very similar to that of amorphous MoS_2 formed by Hu and co-workers from MoS_4^{2-} precursor via cathodic electrolysis [48]. The material here is differentiated though by a higher MoO_3 component indicated by a more significant Mo(VI) signal as well as a substantial oxygen 1 s peak at 530.64 eV [48, 49][3] along with a relatively low Mo:S ratio of 1:1.3. The inordinate amount of MoO_3 contained in the dimer deposit may not stem simply from air oxidation but rather from the deposition process itself. High local concentration of OH^- at the electrode would support oxide formation so the deposition process can be envisioned to include hydrolysis of the dimer's oxo to OH^- by TFA protons. Deposition likely also involves the same type of sulfur rearrangement via HS^- expulsion which occurs in formation of the similar amorphous MoS_2 material [48].

Films deposited from Mo dimer were evaluated as heterogeneous HER catalysts in 0.484 M HCl. Both large surface area films on FTO (0.38 cm^2, Figure S5) and smaller films on glassy carbon (0.071 cm^2) were tested but the

[3] The other signal observed in the O1s region for the dimer electrodeposit (532.2 eV) is consistent with a weakly adsorbed oxygen species such as surface moisture (ref [49]). Although this species cannot be definitively assigned, its weak association makes it unlikely to persist in the electrodeposit and effect HER once exposed to the aqueous catalytic solution. A similar high energy O1s signal can be seen for MoS_2 electrodeposited by Vrubel et al. (ref [48]), but the oxygen region is often not discussed in work with amorphous MoS_x so its prevalence in other catalysts is unclear.

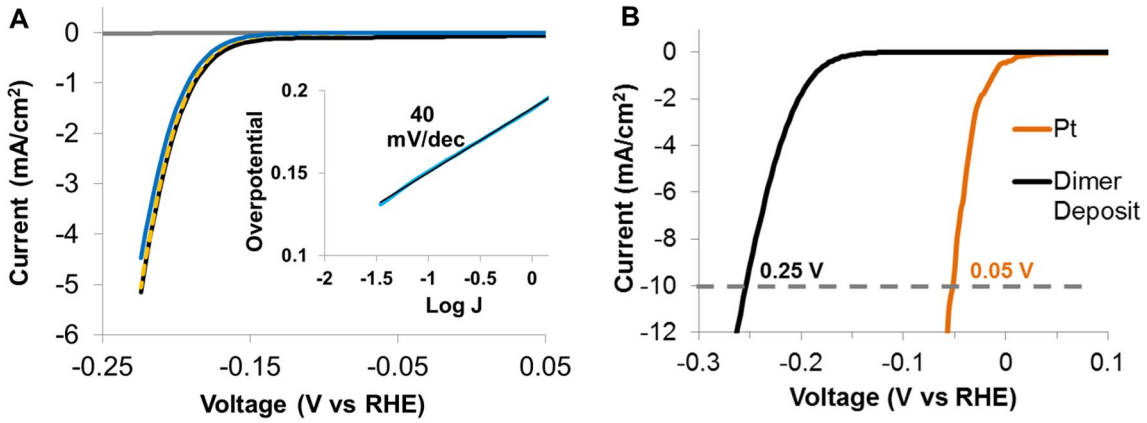

Fig. 4 Linear sweep voltammetry showing the performance of a nafion-protected $[Mo_2O_2S_8]^{2-}$ electrodeposit on glassy carbon in 0.484 M HCl. **a** Consecutive cathodic sweeps (first = black, second = gold dashed, fourth = blue) with the response of bare glassy carbon (grey) shown as a control. The inset displays the Tafel plot derived from the 2nd sweep. **b** Comparison to a commercial platinum disk electrode. Overpotentials required to reach the benchmark 10 mA/cm^2 are indicated. All voltammetry was conducted at 5 mV/s under nitrogen and the employed electrodeposit was formed from DMF solution with 18 equivalents of TFA

performance on glassy carbon was best and will be the focus of discussion. Linear sweep voltammetry on the glassy carbon films shows a strong catalytic response with initial scans, while also showing a more anodic, low current process likely due to the reduction of detected MoO_3. Subsequent scans lack this process indicating the dissolution of MoO_3 in the acidic electrolyte [37]. Scanning also reveals a dramatic loss of catalytic activity accompanied by visible detachment of the films from the electrode (Figure S6). To combat this instability, a protective nafion coating inspired by other MoS_x reports [23, 41] has been applied and enables more stable sweeping (Fig. 4a). Nafion-coated deposits give a reproducible response with voltammograms shifting no more than 9 mV between different films (Figure S7). The average[4] Tafel slope is 40 mV/dec while a current density of 10 mA/cm^2 is reached at an overpotential of 0.25 V. Headspace analysis during electrolysis at an overpotential of 0.23 V reveals an average 98% faradaic efficiency for H_2 generation. However, long-term electrolysis used in the efficiency measurements also reveals that even with the nafion coating, the deposits are unstable over time and lose 73–78% of their initial current density within 60 min (Figure S8).

For the HER performance of the dimer deposit to be compared with other molybdenum sulfides, relative loading must be taken into account. The molybdenum content measured for the deposit here is inflated by the presence of significant, inactive MoO_3, but for a pure phase, it would translate to MoS_2 loading of 18 µg/cm^2 and this can be used as an upper limit. Within the same loading regime at 15 µg/cm^2, amorphous MoS_2 gives a similar HER performance with the same Tafel slope and an overpotential of ~ 0.2 V at 10 mA/cm^2 [30, 48]. This is in good agreement with the structural similarities observed for the two types of electrodeposits and indicates that using the deposition conditions here with the $[Mo_2O_2S_8]^{2-}$ precursor does not provide a distinct advantage over the traditional use of MoS_4^{2-} in water. When comparing the dimer deposit to other prominent electrodeposited molybdenum sulfides, it is slightly less active than Mo_3S_{13} (η = 0.20 V at 10 mA/cm^2, Tafel slope = 37 mV/dec) having a much higher content of sulfur, especially bridging S_2^{2-} [41]. At the same time, the dimer deposit lags much more significantly behind MoS_x/pyrrole co-deposits which are enriched with bridging sulfur and require less than a 60 mV overpotential to reach 10 mA/cm^2 at a low Mo loading of 7.8 µg/cm^2 [23].

Notably, HER behavior reported for the dimer electrodeposit may not represent optimal performance as the deposition process involves a number of parameters which can be tuned. Among these, concentration of added TFA could be expected to affect deposit morphology by influencing the rate of film growth as well as the competition between HER and deposition. TFA concentration effects have been briefly explored here by comparing films made with 1 TFA equivalent per dimer to those discussed above which were made with 18 TFA equivalents. Lowering the TFA equivalents leads to lower deposition currents and a lower Mo loading per unit charge. However, XPS shows no significant change in deposit structure (Figure S9) and HER performance remains similar. The 1-equivalent films reach 10 mA/cm^2 at nearly the same overpotential (0.24 V,

[4] The Tafel slope is the average of measurements from 3 different films while faradaic efficiency is an average from two trials each with four time points.

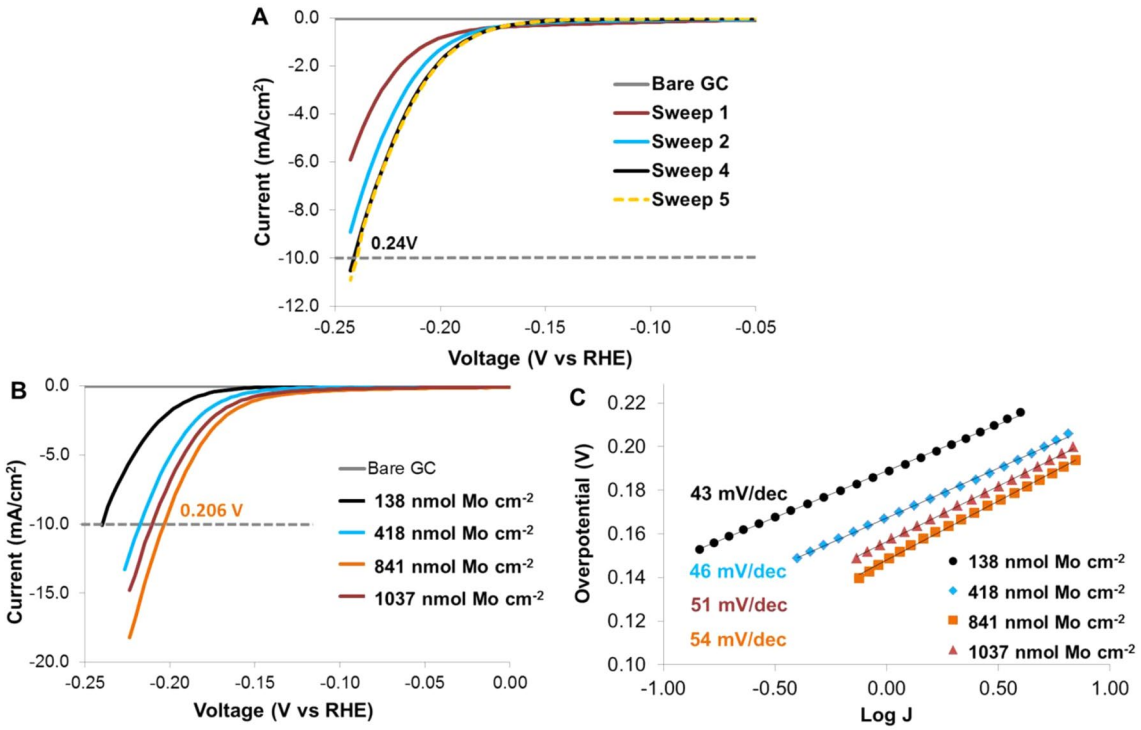

Fig. 5 HER catalysis in 0.484 M HCl by $[Mo_2O_2S_8]^{2-}$ dropcasts on glassy carbon (0.071 cm^2). **a** Consecutive linear sweeps showing cathodic activation of a dropcast having a loading of 138 nmol Mo/cm^2. The response of bare glassy carbon (grey) is shown as a control. **b** Linear sweeps showing the activated performance of dropcasts having different Mo loadings. The grey dotted line denotes the 10 mA/cm^2 benchmark and the overpotential required to achieve this marker is displayed for the best dropcast. **c** Tafel plots and resulting slopes for activated dropcasts of different Mo loading. All linear sweep voltammetry was conducted under nitrogen at 5 mV/s

Figure S10) as 18-equivalent films, while giving a slightly less favorable Tafel slope (42.6 mV/dec) and faradaic efficiency (95.6%) albeit at lower loading. Thus, acid concentration cannot be used to enhance deposit properties; however, the effects of other deposition parameters, such as potential and solvent, remain unexplored.

2.3 Dropcasting

In addition to electrodeposition, simple dropcasting has been explored as a means to form a heterogeneous catalyst from the small molecule dimer $[Mo_2O_2S_8]^{2-}$. Dropcasting was done on glassy carbon substrates (0.071 cm^2) using homogenized DMF suspensions with dimer, nafion, and carbon powder for conductivity. In HCl, the resulting dropcast films give a highly reproducible catalytic HER response summarized in Fig. 5. This response improves dramatically during initial sweeps indicating an activation process. Activated films show the expected impacts of catalyst loading: Catalytic response increases with loading before saturating and then regressing at very high loadings which can cause agglomeration and obstruction of active sites. The maximum performance observed here corresponds to a loading of 841 nmol Mo/cm^2 with a Tafel slope of 54 mV/dec and a 0.21 V overpotential at 10 mA/cm^2. For comparison to the dimer electrodeposits above, a dropcast film was prepared at a similar loading of 138 nmol Mo/cm^2. This dropcast has a lower average faradaic efficiency (87%) than the electrodeposit but reaches 10 mA/cm^2 at nearly the same overpotential (0.24 V, Figure S11) and has a similar Tafel slope of 43 mV/dec (Fig. 5c).

Combined with the observed activation period, the similarity of the dropcast's performance to that of the electrodeposit raises the question of whether the dropcast dimer simply transforms into the electrodeposit structure during the reduction of HER. To address this, XPS has been conducted with a dropcast film on FTO support before and after extended catalysis (Fig. 6).

Before catalysis, the dropcast has all of the features reported previously for the small molecule dimer including signals for bound oxygen (531.36 eV), Mo(V) (234.1/230.96 eV), and terminal/unsaturated sulfur (163.78/162.62 eV) [45]. Expected nafion signals (536.1 eV and 169 eV) [50] are also observed along with two extraneous signals which can be assigned as free

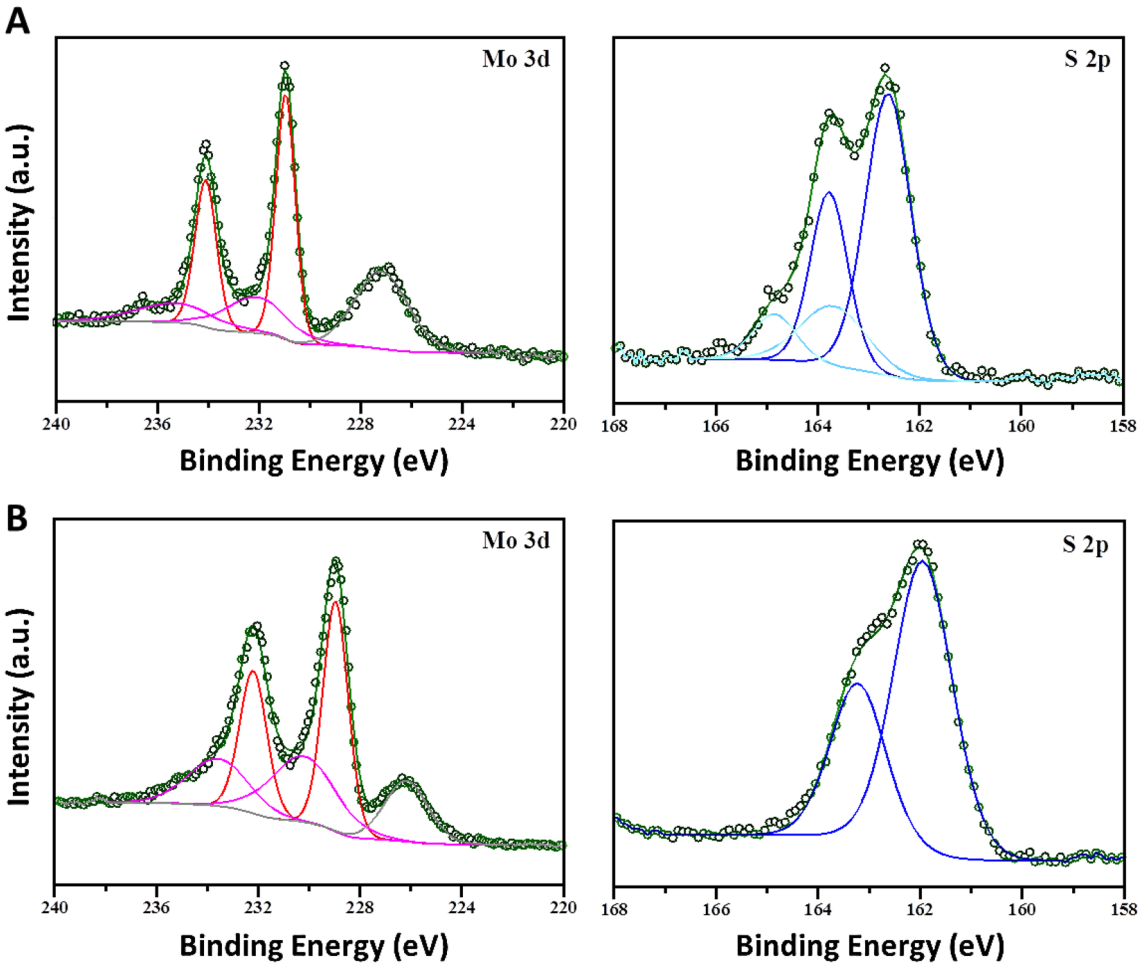

Fig. 6 Comparison of XPS results in the Mo 3d (left) and S 2p (right) regions for a dropcast dimer film on FTO **a** before and **b** after extended HER catalysis

sulfur (164.85/163.69 eV) from dimer synthesis [41, 42, 48] and Mo(VI) from the synthetic starting material or MoO_3 byproduct.[5] XPS after catalysis reveals loss of the free sulfur impurities as well as other significant changes. The signal for Mo bound oxygen near 531.36 eV becomes much less prevalent (see Figure S9B for discussion of O1s region). In the Mo region, some high valent Mo similar to Mo(V) in the dimer is still observed (233.6/230.23 eV), but the major signal appears at 232.2/228.96 eV and is consistent with Mo(IV) in crystalline MoS_2 and electrodeposited MoS_x [37, 48]. Moreover, although the sulfur region continues to show only terminal and unsaturated sulfur, the sulfur binding energy has shifted to lower values (163.22/161.94 eV) found in MoS_2 environments [48]. All of the observed XPS changes suggest that during catalysis, the dropcast dimer transforms from its discrete molecular form to a MoS_2 structure most similar to crystalline MoS_2 lacking bridging or apical sulfur. This transformation is further supported by the Mo:S ratio in the final catalyst which is 1:2.

The shift from the dimer towards an MoS_2 structure closely resembles a transformation observed by Jaramillo's group using dropcast nanoparticles also derived from heptamolybdate starting material [51]. In accordance with this similarity, the catalysts emerging from the two dropcasts achieve comparable HER performance at high loadings. Both ultimately adopt a MoS_2 architecture but dramatically outperform the bulk material in terms of overpotential and Tafel slope [9]. Thus, the approach of dropcasting these discrete compounds proves to be a simple way of forming dispersed MoS_2 with high exposure of active sites.

At the onset of this work, one of the motivations was to further probe the relative activities of different sulfur

[5] MoO_3 is known to form from the same synthetic conditions as $[Mo_2O_2S_8]^{-2}$ with added acid (ref [51]) and thus could be a minor byproduct of dimer synthesis where the molybdate starting material causes a slightly acidic pH.

motifs by comparing the dimer having only terminal and unsaturated sulfur to materials which also include bridging or apical sulfur. In comparison to other dropcast materials, the dimer dropcast lags behind top performing clusters including $[Mo_2S_{12}]^{2-}$ and $[Mo_3S_{13}]^{2-}$ [34, 35]. However, those clusters are believed to remain intact and maintain a high Mo:S ratio during catalysis, so their performance is influenced largely by the number of active sites and not just by the types of sites. When comparing to amorphous electrodeposits with a similar, low Mo:S ratio, turnover frequency per Mo center is an important metric of activity. For the catalyst formed from the dimer dropcast, the initial turnover frequency measured here is 0.2 s^{-1} but this value is a lower limit as it is calculated based on the total dropcast amount of molybdenum rather than confirmed surface accessible sites. Taking this into consideration, the turnover of the dimer dropcast is within the same regime as that of amorphous MoS_2 [10]. On the other hand, however, overpotential and Tafel slope are less favorable for the dimer dropcast [30]. Bridging and apical sulfur in the amorphous material may help to give it the edge over the dropcast but the dissimilar nature of the two materials means that effects from other factors like intrinsic conductivity cannot be ruled out. In the end, the dimer dropcast can only further confirm that strong HER is possible based on terminal/unsaturated sulfur, and catalyst design must target high sulfur content.

2.4 Density functional theory (DFT) calculations

DFT calculations were performed on the molecular dimer (Fig. 1b) in order to simulate its behavior in the presence of protons and electrons. Although homogenous HER is not observed for the molecular dimer, pathways for that process were computed in an effort to explain structural changes observed in the dimer during reduction and the unfavorable nature of the molecular catalysis. All ground-state geometry optimizations were performed with Gaussian 16 [52]. Solvent effects were simulated in DMF with the solvation model density method (SMD) with electrostatics in terms of the integral-equation formalism polarizable continuum model (IEF-PCM) [53–56]. The SMD solvation model is the recommended choice by Gaussian 16 for the change of free energy of solvation. Ground-state geometry optimizations were carried out using the B3LYP [57–59] density functional. The SDD energy consistent pseudopotential was used for the core electrons along with the valence electrons of molybdenum [60] while the 6-31 + G* [61–65] basis set was used for all other atoms. Optimized stationary points were confirmed to be local minima (all real vibrational frequencies) or transition states (one imaginary vibrational frequency) on the potential energy surface using vibrational frequency analysis, and each transition state was connected to its respective reactant and product by intrinsic reaction coordinate (IRC) analyses [66].

HER pathways were proposed for the molecular dimer based on the calculated Gibbs free energy of all potential reactants, intermediates and products. A total of 10 pathways were investigated and are shown in full in the supporting information. These pathways can be separated into three categories based on the ordering of the two protonations and electron injections required for HER. Pathways 1 and 2 adhere to the following ordering of steps: (1) protonation (2) electron injection (3) protonation (4) electron injection. Pathways 3 through 6 follow the order: (1) electron injection (2) protonation (3) protonation (4) electron injection. Pathways 7 through 10 have the order: (1) electron injection (2) protonation (3) electron injection (4) protonation. To account for the stoichiometry changes that occur as a result of protonation, *N*-protonated pyridine was used as a proton source.

Experimental evidence suggests that protons do not interact with the ground state dimer so electron injection should be the first step in any HER pathway; DFT is in agreement with this by indicating that electron injection is the most thermodynamically favorable first step. Pathways 1 and 2 explore the possibility of initial protonation considering both the terminal S_2^{2-} and S_4^{2-} moieties as protonation sites due to their involvement in the HOMO and HOMO-1 orbitals (Fig. 7). However, at both moieties, initial protonation is thermodynamically unfavorable (Figures S16–S18), while initial electron injection (Paths 3–10) is thermodynamically favorable by –68.5 kcal/mol.

Pathways with an initial electron injection step (pathways 3–10) show that this step leads to an "open" $[Mo_2O_2S_8]^{3-}$ trianion species resulting from ring opening of the dimer's terminal S_4^{2-} into an $(S^-)(S_3^-)$ moiety (Fig. 7). After electron injection, the studied pathways consider the possibilities for subsequent proton interaction by focusing on protonation at the $(S^-)(S_3^-)$, unsaturated S_2^{2-}, and oxygen moieties of the "open" $[Mo_2O_2(S_2)(S_2)(S)(S_3)]^{3-}$ species. Although oxygen has been suggested to play an important role in our previous DFT work with small molecule MoS_x mimics [36], any attempt to protonate the oxygen atoms in this catalyst ultimately led to bound protons having unfavorable orientations for subsequent H_2 generation. When considering sulfur protonation, all but one pathway involves an uphill protonation step on the order of ~ 14–20 kcal/mol. Pathway 7 is the only case where all four steps of hydrogen binding to the small molecule dimer are thermodynamically favorable (Figure S25) and it shows formation of a $[Mo_2O_2(S_2)(S_2)(S–H)(S_3–H)]^{2-}$ product as seen in Scheme 1. The transformations seen for the molecular dimer in pathway 7 indicate that the irreversible nature of experimental reductions observed in DMF stems

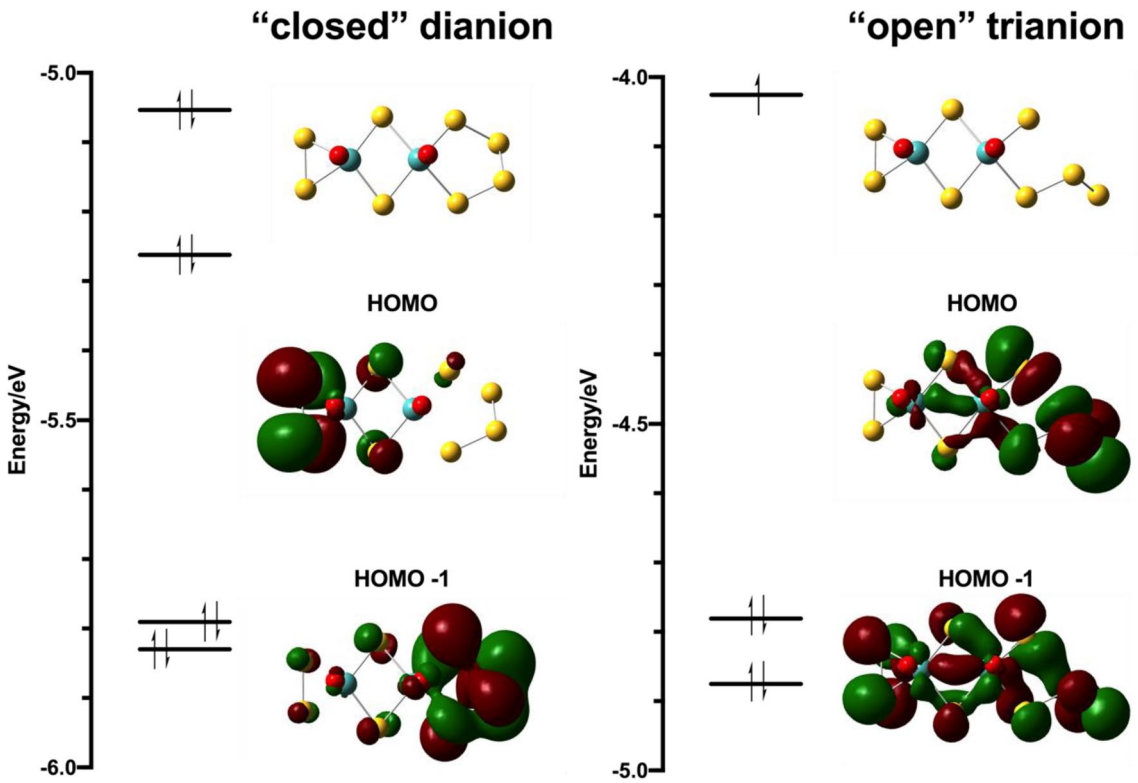

Fig. 7 Comparison of the HOMO and HOMO-1 orbitals of the "closed" $[Mo_2O_2S_8]^{2-}$ species before reduction (left) and the "open" $[Mo_2O_2S_8]^{3-}$ species (right) after electron injection. Suggests initial protonation to occur on the $(S^-)(S_3^-)$ moiety after formation of the "open" trianion species

from ring opening of the dimer's terminal S_4^{2-}. Furthermore, based on pathway 7, reduction in acid likely causes transition to MoS_x through protonation of the reduced "open" dimer to form $[Mo_2O_2(S_2)(S_2)(S–H)(S_3–H)]^{2-}$ which then can allow for SH^- expulsion.

Exhaustive efforts to create a closed HER catalytic cycle from pathway 7 have revealed that no transition state for the HER reaction is accessible from the $[Mo_2O_2(S_2)(S_2)(S–H)(S_3–H)]^{2-}$ species due to the strength of its S–H and S_3–H bonds. Closed cycles in which a HER transition state is observed in the final product are obtained via pathways 2, 5, and 9 (Figures S29–S30). However, as noted above, these pathways involve at least one uphill protonation step. Additionally, the production of molecular hydrogen may result in a singlet or triplet $[Mo_2O_2(S_2)(S_2)(S)(S_3)]^{2-}$ species and only the triplet is able to regenerate $[Mo_2O_2(S_2)(S_2)(S)(S_3)]^{2-}$ via electron injection (Figure S29–S30). Pathway 9 shown in Scheme 2 represents the most likely path to the possible generation of molecular hydrogen with a HER transition state. However, the lack of HER in pathway 7 combined with the uphill protonation steps and the peculiar conditions for catalyst regeneration in pathways 2, 5, and 9 indicate that the catalyst is not active as a molecule. This is in agreement with the experimental observation that all active catalysts derived from the dimer lose their molecular features.

3 Conclusions

The small molecule dimer $[Mo_2O_2S_8]^{2-}$ has been investigated as a possible gateway to HER catalyst materials rich in saturated and terminal sulfur. This dimer shows repeatable reductions in DMF, but in the presence of trifluoroacetic acid, it is not a stable homogeneous catalyst and instead forms an electrodeposit. DFT suggests that the reductive instability results from formation of an "open" $[Mo_2O_2S_8]^{3-}$ trianion which then is protonated in the presence of acid to give a $[Mo_2O_2(S_2)(S_2)(S–H)(S_3–H)]^{2-}$ (Scheme 1) or a $[Mo_2O_2(S_2)(S_2–H)(S–H)(S_3)]^{2-}$ species (Scheme 2). Some computed reaction pathways suggest the possibility of HER from the $[Mo_2O_2(S_2)(S_2–H)(S–H)(S_3)]^{2-}$ species, but no thermodynamically favorable transition state for HER could be accessed from the $[Mo_2O_2(S_2)$

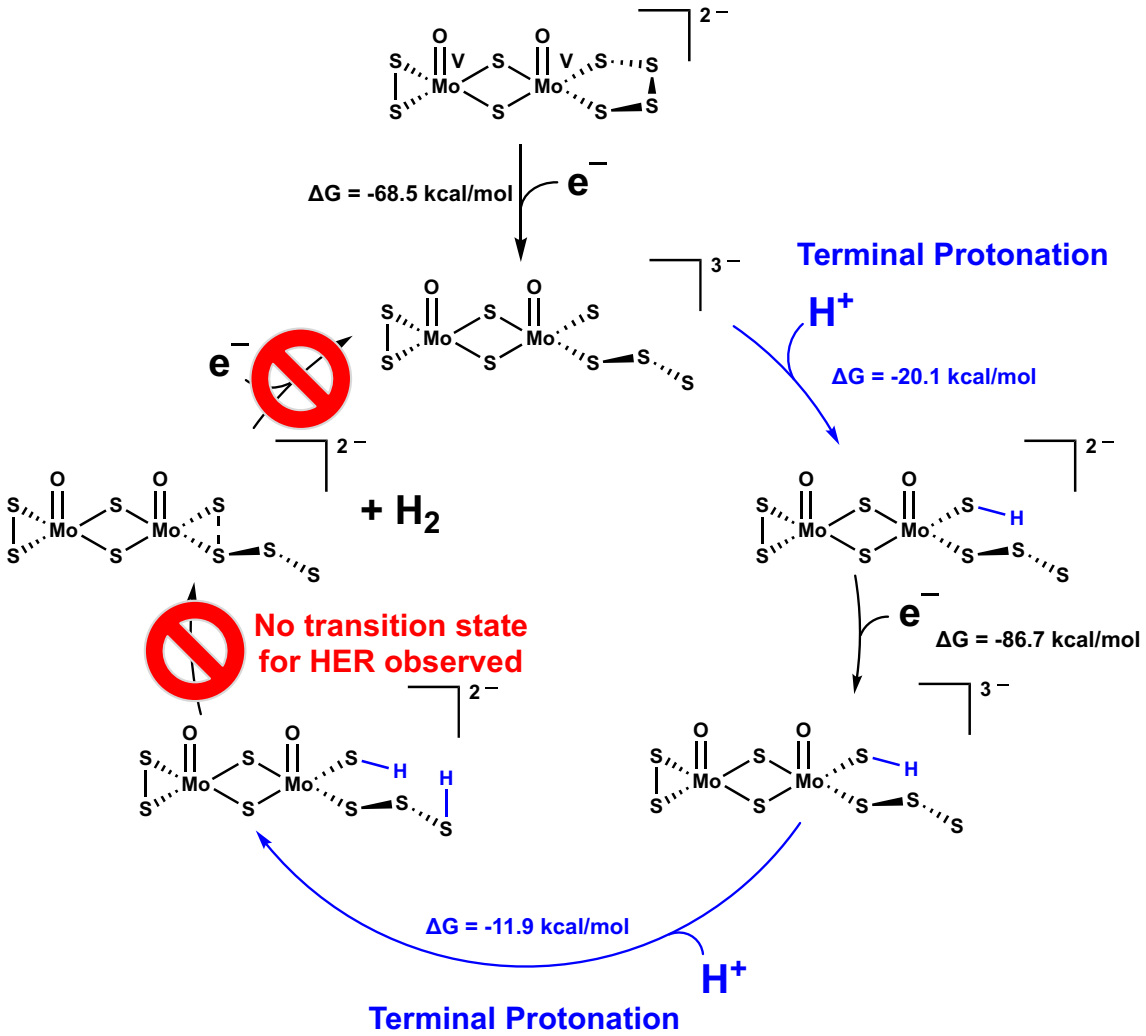

Scheme 1 Pathway 7 for HER catalysis with the corresponding change in Gibbs free energy for each step shown (Figure S25). This pathway follows the reaction path of electron injection (1), protonation of the $(S^{-})(S_3^{-})$ moiety (2), electron injection (3), and protonation of the $(S–H)(S_3^{-})$ moiety (4). No transition state for HER is observed in the final $[Mo_2O_2(S_2)(S_2)(S–H)(S_3–H)]^{2-}$ product

$(S_2)(S–H)(S_3–H)]^{2-}$ reduction product, thus giving one possible explanation for the lack of homogeneous catalysis. Electrodeposit from the dimer does however prove to be a heterogeneous HER catalyst with high faradaic efficiency in aqueous acid. The dimer electrodeposit does not maintain the type or high content of sulfur found in the original dimer and instead is quite similar to electrodeposited amorphous MoS_x. Despite this similarity, the dimer deposits require more overpotential than the more optimized amorphous MoS_x. Initial efforts to tune the amount of acid in the deposition solution did not improve performance, but other deposition parameters could possibly be tuned to realize a better catalyst.

Beyond electrodeposition, the dimer $[Mo_2O_2S_8]^{2-}$ can be converted to a heterogeneous HER catalyst via dropcasting. The dropcast dimer converts away from its molecular form during catalysis; it retains the exclusive terminal/unsaturated character of its sulfur but loses its high S:Mo ratio to adopt an end structure resembling crystalline MoS_2. HER activity is much higher though for the dropcast dimer than bulk MoS_2 showing that dropcasting the dimer is a simple way of obtaining dispersed MoS_2 with high exposure of active terminal/unsaturated sulfur. That being said, the performance of the dropcast dimer cannot match that of dropcast clusters which maintain a higher sulfur content. This supports the current emphasis on sulfur enrichment in molybdenum sulfide design.

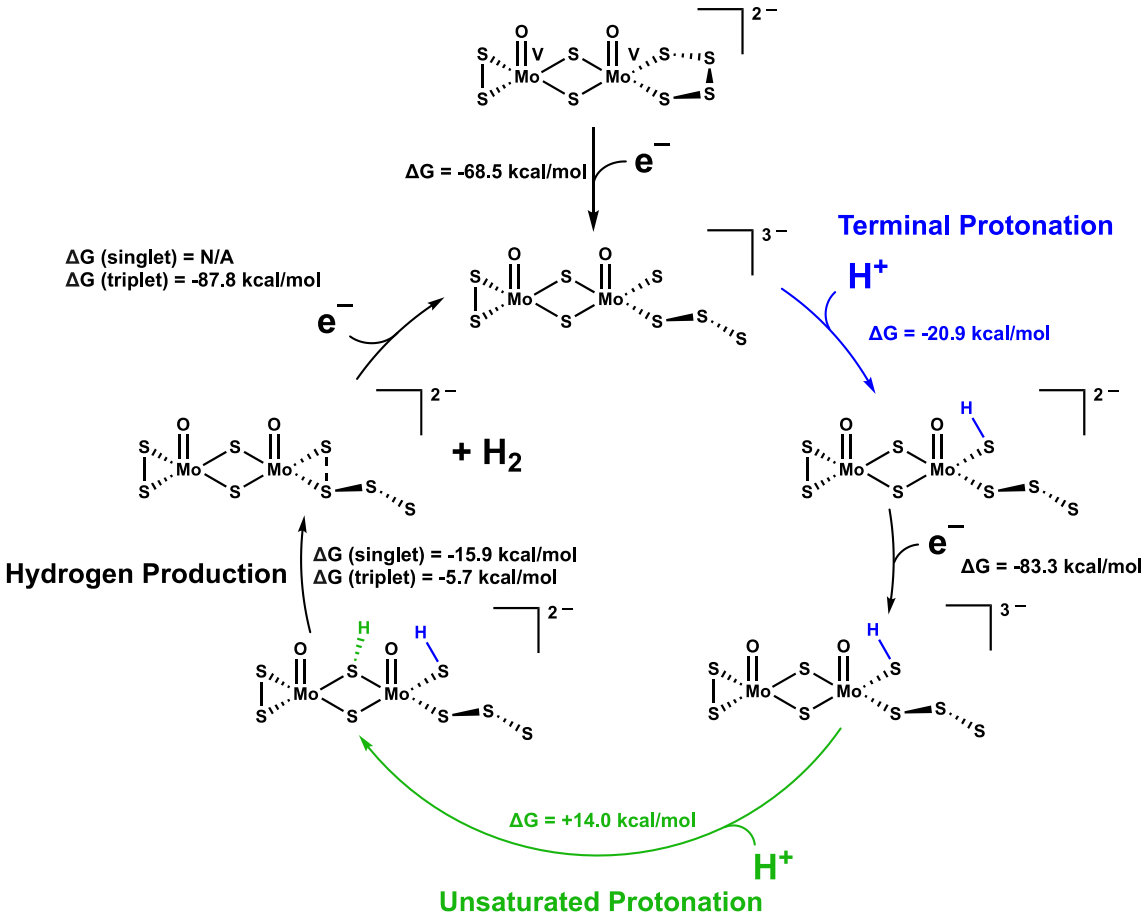

Scheme 2 Pathway 9 for HER catalysis with the corresponding change in Gibbs free energy for each step shown (Figure S27). This pathway follows the reaction path of electron injection (1), protonation of the opened (S^{-})(S_3^{-}) moiety (2), electron injection (3), and protonation of the unsaturated (S_2^{-}) moiety (4). Transition state is observed for the $[Mo_2O_2(S_2)(S_2–H)(S–H)(S_3)]^{2-}$ product to form molecular hydrogen. However, after the hydrogen production step, only the triplet state of the $[Mo_2O_2(S_2)(S_2)(S)(S_3)]^{-2}$ product was able to reproduce the "open", active $[Mo_2O_2(S_2)(S_2)(S)(S_3)]^{3-}$ species suggesting unlikely catalysis

Meanwhile, the dropcast also cannot match performance of amorphous MoS_2 which is not sulfur rich but does have bridging and apical sulfur. Thus, development of a catalyst which is particularly rich in terminal and unsaturated sulfur remains an interesting target for clear comparison to the top performing clusters and electrodeposits rich in bridging and apical sulfur.

Acknowledgements We acknowledge Dr. Lisa Alexander for her help in collecting XPS data as well as Dr. Xin Yang and Congcong Xue for assistance in troubleshooting gas chromatography measurements. We appreciate the assistance of Anthony Lutton in running ICP-OES. We thank Dr. Kevin Click and Dr. William McCulloch for helpful discussions on heterogeneous electrochemical measurements. We also gratefully acknowledge financial support from the NSF Chemistry Catalysis Program of the Chemistry Division—CHE-1566106. We acknowledge generous computational resources from the Ohio Supercomputer Center.

Compliance with ethical standards

Conflict of interest The authors declare no competing financial interest.

References

1. Walter MG, Warren EL, McKone JR, Boettcher SW, Mi Q, Santori EA, Lewis NS (2010) Solar water splitting cells. Chem Rev 110:6446–6473
2. Queyriaux N, Kaeffer N, Morozan A, Chavarot-Kerlidou M, Artero V (2015) Molecular cathode and photocathode materials for hydrogen evolution in photoelectrochemical devices. J Photochem Photobiol C 25:90–105
3. Xu P, McCool NS, Mallouk TE (2017) Water splitting dye sensitized solar cells. Nano Today 14:42–58
4. U.S. Energy Information Administration (2008) The Impact of Increased Use of Hydrogen on Petroleum Consumption and Carbon Dioxide Emissions. https://www.eia.gov/analysis/requests/2008/sroiaf%282008%2904.pdf. Accessed 25 Nov 2019

5. International Energy Agency Hydrogen Technology Collaboration (2017) Global Trends and Outlook for Hydrogen. https://ieahydrogen.org/pdfs/Global-Outlook-and-Trends-for-Hydrogen_Dec2017_WEB.aspx. Accessed 25 Nov 2019
6. Turner JA (2004) Sustainable hydrogen production. Science 305:972–974
7. da Silva Veras T, Mozer TS, dos Santos D, da Silva César A (2017) Hydrogen: trends, production and characterization of the main process worldwide. Int J Hydrog Energy 42:2018–2033
8. Zeng M, Li Y (2015) Recent advances in heterogeneous electrocatalysts for the hydrogen evolution reaction. J Mater Chem A 3:14942–14962
9. Yan Y, Xia B, Xu Z, Wang X (2014) Recent development of molybdenum sulfides as advanced electrocatalysts for hydrogen evolution reaction. ACS Catal 4:1693–1705
10. Benck JD, Hellstern TR, Kibsgaard J, Chakthranont P, Jaramillo TF (2014) Catalyzing the hydrogen evolution reaction (HER) with molybdenum sulfide nanomaterials. ACS Catal 4:3957–3971
11. Hinnemann B, Moses PG, Bonde J, Jørgensen KP, Nielsen JH, Horch S, Chorkendorff I, Nørskov JK (2005) Biomimetic hydrogen evolution: MoS2 nanoparticles as catalyst for hydrogen evolution. J Am Chem Soc 127:5308–5309
12. Jaramillo TF, Jørgensen KP, Bonde J, Nielsen JH, Horch S, Chorkendorff I (2007) Identification of active edge sites for electrochemical H_2 evolution from MoS_2 nanocatalysts. Science 317:100–102
13. Bonde J, Moses PG, Jaramillo TF, Nørskov JK, Chorkendorff I (2009) Hydrogen evolution on nano-particulate transition metal sulfides. Faraday Discuss 140:219–231
14. Merki D, Vrubel H, Rovelli L, Fierro S, Hu X (2012) Fe Co, and Ni ions promote the catalytic activity of amorphous molybdenum sulfide films for hydrogen evolution. Chem Sci 3:2515–2525
15. Xie J, Zhang H, Li S, Wang R, Sun X, Zhou M, Zhou J, Lou XW, Xie Y (2013) Defect-Rich MoS2 ultrathin nanosheets with additional active edge sites for enhanced electrocatalytic hydrogen evolution. Adv Mater 25:5807–5813
16. Yan Y, Xia BY, Ge X, Liu Z, Wang J-Y, Wang X (2013) Ultrathin MoS_2 nanoplates with rich active sites as highly efficient catalyst for hydrogen evolution. ACS Appl Mater Interfaces 5:12794–12798
17. Guo J, Li F, Sun Y, Zhang X, Tang L (2015) Oxygen-incorporated MoS_2 ultrathin nanosheets grown on graphene for efficient electrochemical hydrogen evolution. J Power Sources 291:195–200
18. Li G, Chen Z, Li Y, Zhang D, Yang W, Liu Y, Cao L (2020) Engineering substrate interaction to improve hydrogen evolution catalysis of monolayer MoS_2 films beyond Pt. ACS Nano 14(2):1707–1714
19. Liao L, Zhu J, Bian X, Zhu L, Scanlon MD, Girault HH, Liu B (2013) MoS_2 formed on mesoporous graphene as a highly active catalyst for hydrogen evolution. Adv Funct Mater 23:5326–5333
20. Kim J, Byun S, Smith AJ, Yu J, Huang J (2013) Enhanced electrocatalytic properties of transition-metal dichalcogenides sheets by spontaneous gold nanoparticle decoration. J Phys Chem Lett 4(8):1227–1232
21. Li DJ, Maiti UN, Lim J, Choi DS, Lee WJ, Oh Y, Lee GY, Kim SO (2014) Molybdenum sulfide/N-doped CNT forest hybrid catalysts for high-performance hydrogen evolution reaction. Nano Lett 14:1228–1233
22. Hyeon Y, Jung S-H, Jang W, Kim M, Kim B-S, Lee J-H, Nandanapalli KR, Jung N, Whang D (2019) Unraveling the factors affecting the electrochemical performance of MoS2–carbon composite catalysts for hydrogen evolution reaction: surface defect and electrical resistance of carbon supports. ACS Appl Mater Interfaces 11:5037–5045
23. Wang T, Zhuo J, Du K, Chen B, Zhu Z, Shao Y, Li M (2014) Electrochemically fabricated polypyrrole and MoS_x copolymer films as a highly active hydrogen evolution electrocatalyst. Adv Mater 26:3761–3766
24. Li Y, Wang H, Xie L, Liang Y, Hong G, Dai H (2011) MoS_2 nanoparticles grown on graphene: an advanced catalyst for the hydrogen evolution reaction. J Am Chem Soc 133:7296–7299
25. Jiang Y, Li X, Yu S, Jia L, Zhao X, Wang C (2015) Reduced graphene oxide-modified carbon nanotube/polyimide film supported MoS2 nanoparticles for electrocatalytic hydrogen evolution. Adv Func Mater 25(18):2693–2700
26. Kibsgaard J, Chen Z, Reinecke BN, Jaramillo TF (2012) Engineering the surface structure of MoS_2 to preferentially expose active edge sites for electrocatalysis. Nat Mater 11:963–969
27. Jia X, Ren H, Hu H, Song Y-F (2020) 3D Carbon foam supported edge-rich N-doped MoS_2 nanoflakes for enhanced electrocatalytic hydrogen evolution. Chem Eur J 26:1–8
28. Qiao S, Zhang B, Li Q, Li Z, Wang W, Zhao J, Zhang X, Hu Y (2019) Pore surface engineering of covalent triazine frameworks@ MoS_2 electrocatalyst for the hydrogen evolution reaction. ChemSusChem 12(22):5032–5040
29. Huang N, Ding Y, Yan S, Yang L, Sun P, Huang C, Sun X (2019) Ultrathin MoS2 nanosheets vertically grown on CoS_2 acicular nanorod arrays: a synergistic three-dimensional shell/core heterostructure for high-efficiency hydrogen evolution at full pH. ACS Appl Energy Mater 2(9):6751–6760
30. Morales-Guio CG, Hu X (2014) Amorphous molybdenum sulfides as hydrogen evolution catalysts. Acc Chem Res 47:2671–2681
31. Karunadasa HI, Montalvo E, Sun Y, Majda M, Long JR, Chang CJ (2012) A molecular MoS_2 edge site mimic for catalytic hydrogen generation. Science 335(6069):698–702
32. Garrett BR, Click KA, Durr CB, Hadad CM, Wu Y (2016) [MoO(S2)2L]1– (L = picolinate or pyrimidine-2-carboxylate) complexes as MoS_x-inspired electrocatalysts for hydrogen production in aqueous solution. J Am Chem Soc 138(41):13726–13731
33. Garrett BR, Polen SM, Click KA, He M, Huang Z, Hadad CM, Wu Y (2016) Tunable molecular MoS_2 edge-site mimics for catalytic hydrogen production. Inorg Chem 55(8):3960–3966
34. Huang Z, Luo W, Ma L, Yu M, Ren X, He M, Polen S, Click K, Garrett B, Lu J, Amine K, Hadad C, Chen W, Asthagiri A, Wu Y (2015) Dimeric [Mo2S12]2 − cluster: a molecular analogue of MoS2 edges for superior hydrogen-evolution electrocatalysis. Angew Chem Int Ed 54(50):15181–15185
35. Kibsgaard J, Jaramillo TF, Besenbacher F (2014) Building an appropriate active-site motif into a hydrogen-evolution catalyst with thiomolybdate $[Mo_3S_{13}]^{2-}$ clusters. Nat Chem 6(3):248–253
36. Garrett BR, Polen SM, Pimplikar M, Hadad CM, Wu Y (2017) Anion-Redox mechanism of $MoO(S_2)_2$(2,2′-bipyridine) for electrocatalytic hydrogen production. J Am Chem Soc 139(12):4342–4345
37. Deng Y, Ting LRL, Neo PHL, Zhang YJ, Peterson AA, Yeo BS (2016) Operando raman spectroscopy of amorphous molybdenum sulfide (MoS_x) during the electrochemical hydrogen evolution reaction: identification of sulfur atoms as catalytically active sites for H+ reduction. ACS Catal 6(11):7790–7798
38. Lauritsen JV, Kibsgaard J, Helveg S, Topsøe H, Clausen BS, Laegsgaard E, Besenbacher F (2007) Size-dependent structure of MoS2 nanocrystals. Nat Nanotechnol 2:53–58
39. Hu J, Huang B, Zhang C, Wang Z, An Y, Zhou D, Lin H, Leung MKH, Yang S (2017) Engineering stepped edge surface structures of MoS_2 sheet stacks to accelerate the hydrogen evolution reaction. Energy Environ Sci 10:593–603
40. Lassalle-Kaiser B, Merki D, Vrubel H, Gul S, Yachandra VK, Hu X, Yano J (2014) Evidence from in situ X-ray absorption spectroscopy for the involvement of terminal disulfide in the reduction of protons by an amorphous molybdenum sulfide electrocatalyst. J Am Chem Soc 137(1):314–321
41. Du K, Zheng L, Wang T, Zhuo J, Zhu Z, Shao Y, Li M (2017) Electrodeposited Mo_3S_{13} films from $(NH_4)_2Mo_3S_{13}{\cdot}2H_2O$ for

electrocatalysis of hydrogen evolution reaction. ACS Appl Mater Interfaces 9(22):18675–18681
42. Duong TM, Nguyen PD, Nguyen AD, Le LT, Nguyen LT, Pham HV, Tran PD (2019) Insights into the electrochemical polymerization of $[Mo_3S_{13}]^{2-}$ generating amorphous molybdenum sulfide. Chem Eur J 25:13676–13682
43. Coucouvanis D, Hadjikyriacou A, Toupadakis A, Koo S-M, Ileperuma O, Draganjac M, Salifoglou A (1991) Studies of the reactivity of binary thio- and tertiary oxothiomolybdates toward electrophiles. Inorg Chem 30:754–767
44. Coucouvanis D, Toupadakis A, Hadjikyriacou A (1988) Synthesis of thiomolybdenyl complexes with $[Mo_2(S)_2(0)_2]^{2+}$ cores and substitutionally labile ligands. Crystal and molecular structure of the $[Mo_20_2S_4(DMF)_3]$ Complex. Inorg Chem 27:3272–3273
45. Bhattacharyya R, Chakrabarty PK, Ghosh PN, Mukherjee AK, Podder D, Mukherjee M (1991) Reaction of Mo04 2- and W042- with aqueous polysulfides: synthesis, structure, and electrochemistry of η2-polysulfido complexes containing a bridging S, S {M202S2}2 + (M = Mo, W) core. Inorg Chem 30:3948–3955
46. Vincent SP (1979) Oxidation–reduction potentials of molybdenum and iron–sulphur centres in nitrate reductase from *Escherichia coli*. Biochem J 177:757–759
47. Click KA, Beauchamp DR, Huang Z, Chen W, Wu Y (2016) Membrane-inspired acidically stable dye-sensitized photocathode for solar fuel production. J Am Chem Soc 138(4):1174–1179
48. Vrubel H, Hu X (2013) Growth and activation of an amorphous molybdenum sulfide hydrogen evolving catalyst. ACS Catal 3(9):2002–2011
49. Dupin J-C, Gonbeau D, Vinatier P, Levasseur A (2000) Systematic XPS studies of metal oxides, hydroxides, and peroxides. Phys Chem Chem Phys 2:1319–1324
50. Chen C, Levitin G, Hess DW, Fuller TF (2007) XPS investigation of Nafion membrane degradation. J Power Sources 169(2):288–295
51. Benck JD, Chen Z, Kuritzky LY, Forman AJ, Jaramillo TF (2012) Amorphous molybdenum sulfide catalysts for electrochemical hydrogen production: insights into the origin of their catalytic activity. ACS Catal 2(9):1916–1923
52. Frisch MJ et al (2016) Gaussian 16, Rev. A.03. Gaussian Inc., Wallingford CT
53. Miertuš S, Scrocco E, Tomasi J (1981) Electrostatic interaction of a solute with a continuum. A direct utilization of ab initio molecular potentials for the prevision of solvent effects. Chem Phys 55:117–129. https://doi.org/10.1016/0301-0104(81)85090-2
54. Miertuš S, Tomasi J (1982) Approximate evaluations of the electrostatic free energy and internal energy changes in solution processes. Chem Phys 65:239–245. https://doi.org/10.1016/0301-0104(82)85072-6
55. Pascual-Ahuir JL, Silla E, Tunon I (1994) GEPOL: an improved description of molecular-surfaces. 3. A new algorithm for the computation of a solvent-excluding surface. J Comput Chem 15:1127–1138. https://doi.org/10.1002/jcc.540151009
56. Marenich AV, Cramer CJ, Truhlar DG (2009) Universal solvation model based on solute electron density and on a continuum model of the solvent defined by the bulk dielectric constant and atomic surface tensions. J Phys Chem B 113:6378–6396. https://doi.org/10.1021/jp810292n
57. Becke AD (1993) Density-functional thermochemistry. III. The role of exact exchange. J Chem Phys 98:5648–5652. https://doi.org/10.1063/1.464913
58. Stephens PJ, Devlin FJ, Chabalowski CF, Frisch MJ (1994) Ab Initio calculation of vibrational absorption and circular dichroism spectra using density functional force fields. J Phys Chem 98:11623–11627. https://doi.org/10.1021/j100096a001
59. Kim K, Jordan KD (1994) Comparison of density functional and MP2 calculations on the water monomer and dimer. J Phys Chem 98:10089–10094. https://doi.org/10.1021/j100091a024
60. Nicklass A, Dolg M, Stoll H, Preuss H, Nicklass A, Dolg M, Stoll H (1995) Ab initio energy-adjusted pseudopotentials for the noble gases Ne through Xe: calculation of atomic dipole and quadrupole polarizabilities. J Chem Phys 102:8942–8952. https://doi.org/10.1063/1.468948
61. Ditchfield R, Hehre WJ, Pople JA (1971) Self-consistent molecular-orbital methods. IX. An extended gaussian-type basis for molecular-orbital studies of organic molecules. J Chem Phys 54:724–728. https://doi.org/10.1063/1.1674902
62. Hehre WJ, Ditchfield K, Pople JA (1972) Self-consistent molecular orbital methods. XII. Further extensions of gaussian-type basis sets for use in molecular orbital studies of organic molecules. J Chem Phys 56:2257–2261. https://doi.org/10.1063/1.1677527
63. Hariharan PC, Pople JA (1974) Accuracy of AHn equilibrium geometries by single determinant molecular orbital theory. Mol Phys 27:209–214. https://doi.org/10.1080/00268977400100171
64. Gordon MS (1980) The isomers of silacyclopropane. Chem Phys Lett 76:163–168. https://doi.org/10.1016/0009-2614(80)80628-2
65. Hariharan PC, Pople JA (1973) The influence of polarization functions on molecular orbital hydrogenation energies. Theor Chim Acta 28:213–222. https://doi.org/10.1007/BF00533485
66. Gonzalez C, Schlegel HB (1990) Reaction path following in mass-weighted internal coordinates. J Phys Chem 94:5523–5527. https://doi.org/10.1021/j100377a021